Molecular Dynamics of Matrix-Assisted Laser Desorption of Leucine Enkephalin Guest Molecules from Nicotinic Acid Host Crystal

Xiongwu Wu, Mehrnoosh Sadeghi, and Akos Vertes*

Department of Chemistry, George Washington University, Washington, D.C. 20052

Received: January 6, 1998; In Final Form: April 1, 1998

Molecular dynamics simulations of matrix-assisted laser desorption ionization (MALDI) were conducted using a detailed description of the internal degrees of freedom for both matrix (nicotinic acid) and guest (leucine enkephalin) molecules. Afforded by the separate treatment of matrix and guest properties, the energy transfer and the conformation dynamics were followed throughout the desorption process. The effect of the initial matrix temperature and the influence of guest molecule burial depth and charge state were investigated. Elevating the initial temperature of the matrix increased the desorption velocity of the guest molecules, but only a small change in their postdesorption internal temperature was seen. This observation may account for the lack of thermodecomposition of large guest molecules in MALDI. The liftoff velocity of the guest molecules dropped significantly as the burial depth was increased from 5 to 20 Å, indicating that the guest molecules located near the surface entered the plume with higher kinetic energy. Unexpectedly, the guest internal temperatures showed little correlation with the burial depth. The charge state of the guest molecule had a profound effect on the guest conformation after desorption. For the zwitterionic molecule the end-to-end distance decreased from 16.9 ± 0.3 Å to 2.6 ± 0.1 Å in ∼15 ps, whereas for the protonated molecule the end-to-end distance reached its 4.8 ± 0.2 Å equilibrium value in ∼27 ps. The larger fluctuations in the latter case indicate that the protonated molecule has a less rigid structure.

Introduction

Over the past few decades, laser desorption (LD) and volatilization methods have proven to be efficient in producing gas-phase molecular and ionic species for spectroscopic investigations, e.g., mass spectrometry,[1−5] optical spectroscopy in supersonic jets,[6,7] and ion mobility measurements.[8−10] Among these methods, LD mass spectrometry is the most widespread application. Early experiments have already shown, however, that with direct LD methods there is an upper limit to the size of intact molecules that can be desorbed. This limitation is due to the fact that the laser irradiance needed for the desorption of large molecules exceeds the irradiance associated with their decomposition.

The matrix-assisted laser desorption ionization (MALDI) method circumvents this difficulty by embedding the large guest molecules into a host crystal with low phase transition temperature and strong absorption at the laser wavelength.[3] Thus, energizing the sample with the laser leads to the breakdown of the host crystal and to the release of guest molecules. Contrary to the direct LD phenomenon, the MALDI process does not seem to have a molecular weight cutoff. Proteins and synthetic polymers as large as 500 000 amu have been volatilized successfully by MALDI.[11]

Despite its success in intact protein volatilization, MALDI leads to the fragmentation of other types of macromolecules, most notably nucleic acids. The discovery of new matrixes[12,13] and the introduction of delayed ion extraction,[14,15] however, has overcome the stability and resolution problems and dramatically increased the available mass range and versatility of this method. As a consequence, MALDI has been applied to a broad range of gas-phase studies on macromolecular ions, e.g., determining their mass with high (0.05%) accuracy,[16] obtaining information on their conformation,[8−10] and exploring their noncovalent interactions.[17,18] Extensive investigations have been carried out to explore the effect of matrix properties,[19] laser intensity and beam profile,[20] and guest molecule proton affinity[21] on the efficiency of guest ion production.

Inspired by the widespread application and success of MALDI in the volatilization/ionization of biomolecules, several models have been developed to describe individual aspects of the method.[22−25] In an attempt to explain the absence of fragmentation in large guest molecules volatilized by MALDI, the *homogeneous bottleneck model* has been introduced.[22,26] This model shows that due to a frequency mismatch between the internal modes of guest molecules and the host lattice vibrations, an energy-transfer bottleneck exists. This phenomenon may be responsible for the intact volatilization of certain guest species.

In the complementary *cool plume model* Vertes et al. have described the characteristics of the plume generated in the desorption process (i.e., expansion velocity, plume density, and temperature).[23] Solving the hydrodynamic conservation equations for typical MALDI conditions, the absence of thermal degradation is rationalized by expansion cooling of the plume.

A comparison of three different phenomenological ejection models, including the *pressure pulse model*, has been presented by Johnson.[24] Total ion yields, the effect of averaging over a Gaussian laser beam profile, and guest/matrix molecular ion yields are evaluated in this study.

In an attempt to extract information at the microscopic level molecular dynamics (MD) simulations have been applied to the

* Corresponding author. Phone: (202) 994-2717. Fax: (202) 994-5873. E-mail: vertes@gwu.edu.

S1089-5647(98)00636-1 CCC: $15.00
Published on Web 05/22/1998

description of laser desorption.[27−29] Holme and Levine have used MD simulations to study the mechanisms of energy partitioning in direct LD of a diatomic molecule from a cold cluster of 19 Pt atoms.[27] They have showed that for physisorbed systems an energy-transfer bottleneck exists between the surface−adsorbate motion and the internal vibrations, whereas for van der Waals bonds such a bottleneck is absent. Their results also indicate that the surface motions play the primary role in the energy transfer.

For the elucidation of the role internal degrees of freedom play in MALDI, MD studies have been conducted by Vertes and co-workers.[30,31] They investigated the desorption dynamics of guest and matrix molecules including their interaction and the energy transfer involved. These studies supported the idea of an energy-transfer bottleneck between matrix and guest.[22,26] More recently Garrison and co-workers have developed a breathing sphere model to describe the laser desorption and ablation of organic molecules.[32] Their results showed the existence of a threshold fluence separating two mechanisms for the ejection of structureless molecules: surface vaporization leading to desorption at low laser fluences and collective ejection leading to ablation at higher fluences.

Previous attempts to describe MALDI using MD either used severe system size restrictions (i.e., the hemispherical sample volume in refs 30 and 31) or employed reduced representation of the internal degrees of freedom (i.e., the structureless particles in ref 32) to decrease computational complexity. In the present study we account for most of the internal degrees of freedom in the system and apply two-dimensional periodic boundary conditions to represent an extended surface area, thus reducing the limitations of previous models.

It is well-known that sample preparation methods and laser irradiance significantly affect the desorption and ionization processes in MALDI.[33,34] Sample preparation is based on cocrystallization, whereby the growing host crystal embeds the guest molecules. Upon laser energy deposition, the evaporating host releases the embedded guest particles. The presented MD simulations allow us to explore both the embedding and the desorption processes in some detail.

Capitalizing on the detailed representation of molecular structure in our model, we investigate the conformation of a moderately sized peptide embedded in a crystal of small organic molecules. The charge state of the guest particle plays an important role, especially in the case of mass spectrometric detection. To address some of the issues in the long-standing debate about preformed ions versus gas-phase ionization in MALDI, both zwitterionic and protonated guest molecules will be considered. It is, however, an important caveat of our model that the ionization process itself cannot be treated. Thus, we are not able to discuss the ionization mechanism, only assume two possible outcomes of such mechanisms. Moreover, we represent the laser energy deposition by a certain internal temperature rise of the host molecules. The degree of this temperature jump is somewhat arbitrary, although some justification of the selected values is given in the Results and Discussion section.

Conformational studies of gas-phase macromolecular ions have recently experienced an upsurge of interest.[9,35−37] Experimental mobilities obtained from ion chromatography of MALDI-generated ions can be compared to values provided by molecular mechanics calculations. This comparison may unveil certain features of the gas-phase molecular conformation.[9] Our model enables us to follow conformation changes during the desorption process.

The effect of laser irradiance and energy deposition is represented through the influence of matrix temperature histories in our model. We hope to uncover the partitioning between the kinetic and internal energies of the guest particles and their relation to the stability and the measured kinetic energy distributions of desorbed ions. These quantities offer the possibility of comparisons with experimental observables such as the velocity distributions of the desorbed neutrals and ions and the degree of fragmentation in the mass spectrum.

Modeling Methods

All MD calculations were carried out using a recent version of the CHARMM code (version c24b2, CHARMM Development Project, Harvard University, Cambridge, MA) originally developed to describe protein folding in aqueous environment.[38] In pilot calculations no significant difference was observed between the key structural features of the system using the "all-atom" and "extended atom" representations; thus, the extended atom model was used throughout to reduce computational complexity. In this representation, the nonpolar hydrogen atoms are united with the heavy atoms (usually carbon atoms) to form extended atoms, whereas the polar hydrogen atoms are explicitly represented. The empirical potential energy function, $V(\underline{r}_1,\underline{r}_2,...,\underline{r}_N)$, consists of bond stretching, bending, improper dihedral, dihedral, van der Waals, and electrostatic energy terms:

$$V(\underline{r}_1,\underline{r}_2,...,\underline{r}_N) = \sum_{\text{bonds}} k_b(b - b_0)^2 + \sum_{\text{angles}} k_\theta(\theta - \theta_0)^2 + \sum_{\substack{\text{improper}\\ \text{dihedrals}}} k_\omega(\omega - \omega_0)^2 + \sum_{\text{dihedrals}} k_\phi[1 + \cos(n\phi)] + \sum_{\text{pairs}(i,j)} \left(\frac{A_{ij}}{r_{ij}^{12}} - \frac{B_{ij}}{r_{ij}^{6}}\right) S(r_{ij},r_{\text{on},r}\text{off}) + \sum_{\text{pairs}(i,j)} \frac{q_i q_j}{4\pi\epsilon_0\epsilon_r r_{ij}} S(r_{ij},r_{\text{on}},r_{\text{eff}}) \quad (1)$$

where b, θ, ω, b_0, θ_0, and ω_0 represent the bond lengths, bond angles, improper torsion angles, and their equilibrium values, respectively. The torsion angle and the corresponding force constant are represented by ϕ and k_ϕ. Force constants for stretching, k_b, bending, k_θ, and improper torsion, k_ω, are distinguished according to the participating atoms and the nature of their bonding. The last two terms describe the pairwise van der Waals and electrostatic interactions. Since the electrostatic term tends to dominate the energy equation, the validity of the description hinges on the proper selection of the q_i partial charges attributed to the atoms (see later). To keep the computational requirements at bay, a cutoff is introduced for the nonbonded interactions in the form of a switching function, $S(r_{ij},r_{on},r_{off})$. In the presented simulations, the forces stemming from the nonbonded interactions are smoothly switched to zero in the range from r_{on} to r_{off}. No explicit hydrogen bonding term was used.

The structure of nicotinic acid was represented as a 10-atom molecule shown below:

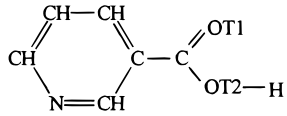

Since the original CHARMM parameter files did not provide the force constants for the atoms in nicotinic acid, we estimated the bonding and van der Waals parameters by analogy using similar compounds and groups in the CHARMM force field database. Wave functions and partial charges on the atoms were

calculated using the GAMESS ab initio program for the fully optimized structure at the 6-31G* level.[39] Details of the force field parameter estimation have been described elsewhere.[30,31]

Based on X-ray diffraction data the nicotinic acid crystal structure is described as a monoclinic lattice with lattice parameters $a = 7.715 \pm 0.002$ Å, $b = 11.682 \pm 0.002$ Å, $c = 7.220 \pm 0.002$ Å, $\alpha = 90°$, $\beta = 113° 23' \pm 3'$, and $\gamma = 90°$.[40,41] The initial conditions in our simulations were based on this structure. In the presented calculations the unit cell was repeated five times in the x and z directions and three times in the y direction to build a box of 300 nicotinic acid molecules in 10 layers. The obtained matrix crystal segment was energy minimized for 100 steps with the adopted basis Newton−Raphson method and equilibrated at 300 K for 100 ps with three-dimensional (3D) periodic boundary conditions. The resulting structure was used as a building block in the simulations.

In our previous stochastic boundary MD studies a hemispherical volume ($\varnothing \approx 5 \times 10^{-3}$ μm) of nicotinic acid molecules was simulated with a leucine enkephalin guest particle embedded under the surface.[30,31] Compared to the typical laser spot size in a MALDI experiment ($\varnothing \approx 10$ μm), however, the simulated surface area was rather small. To alleviate this limitation and maintain the calculations at a manageable level, we departed from the stochastic boundary conditions and the hemispherical geometry and adopted the two-dimensional (2D) periodic boundary conditions. These modifications allowed us to account for a substantial segment of the MALDI sample that interacts with the laser radiation.

The 2D periodic boundary condition was accomplished by using the image facility in CHARMM and translating the system along the $x-y$ plane.[42] Such a periodic treatment made our simulation system behave like an infinite large system along the x−y plane. With the 2D periodic boundary condition only along the $x-y$ plane, however, the system could evaporate in the positive z direction. On the z axis, the top surface represented the solid−vacuum interface where only the interactions on the crystal side were present. On the other boundary, several layers of nicotinic acid molecules were restricted in their motion to mimic the crystal in the negative half space. The direct description in the $x-y$ direction was limited to the size of the modeled area, 35.6 Å × 35.0 Å. If a molecule moved out of the boundaries in the x or y direction, its image entered the system from the opposite side. Thus, the 2D density of the system was kept constant. The average 3D density, however, decreased as the evaporation proceeded.

The thickness of the static layer at the bottom had to be enough to allow for the interaction with the energized molecules, i.e., had to be commensurate with the cutoff distance of nonbonded interactions. This condition allowed the molecules in the constrained layers to interact with the molecules involved in the desorption process. Figure 1 shows the equilibrium configuration of the host−guest system at 300 K. Throughout the calculations the nonbonded, van der Waals, and electrostatic interactions were cut off at 14.0 Å. Therefore, two layers of nicotinic acid molecules at the bottom boundary were fixed to mimic the bulk of the crystal.

In the simulations the leucine enkephalin guest molecule was represented in two different charge states, the zwitterionic form,

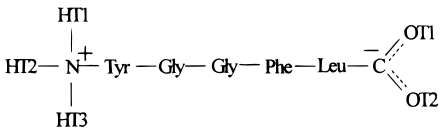

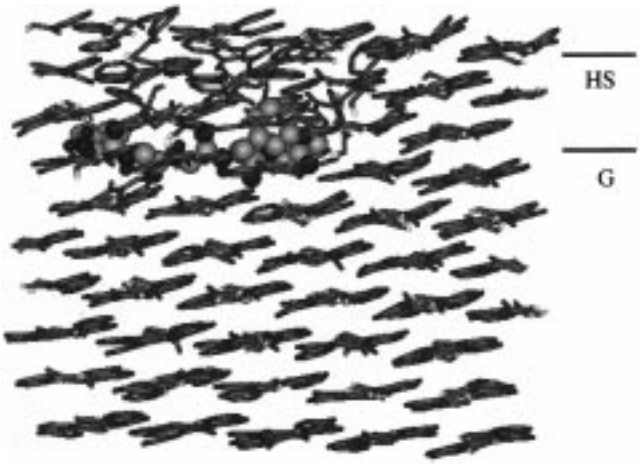

Figure 1. Average conformation of a zwitterionic leucine enkephalin guest molecule embedded 10 Å below the surface of the nicotinic acid host crystal at 300 K. The bottom two layers of nicotinic acid molecules are constrained to mimic the bulk nicotinic acid crystal. HS indicates the position of the host surface, whereas G stands for the guest center-of-mass position.

and the protonated form,

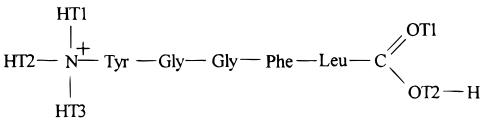

leucine enkephalin molecule (zwitterionic and protonated) were taken directly from the CHARMM force field database.

A fully extended leucine enkephalin species was inserted into the equilibrated matrix crystal. Beavis and Bridson had studied the inclusion of protein molecules in single crystals of *trans*-3,5-dimethyoxy-4-hydroxycinnamic acid (sinapinic acid).[43] They showed that the protein molecules were included along the crystal faces parallel to the hydrogen-bonded sheets of sinapinic acid matrix molecules. Because of the structural similarities between nicotinic acid and sinapinic acid crystals, we assumed that the inclusion of peptide molecules in nicotinic acid was similar to that in sinapinic acid matrix. The leucine enkephalin molecule was embedded parallel to the layers of nicotinic acid molecules at varying depths. All the overlapping nicotinic acid molecules in a radius of 2.6 Å around the guest molecule were deleted from the system. After the insertion of the guest particle, the system was energy minimized and reequilibrated at 300 K for 100 ps (see Figure 1).

The laser energy in a MALDI experiment is considered to be absorbed primarily by the matrix molecules. To simulate the laser excitation of mainly the matrix molecules, we chose the multibath Nose−Hoover method for temperature control.[44,45] The energy flow from the heat bath to the particles in the simulation was governed by the thermal inertial parameter, η. To describe the different initial energy deposition into matrix and guest molecules, the coupling constants between the heat bath and the two species were different. The chosen values for η in both cases were those recommended by the Nose−Hoover method described in the CHARMM manual. The value for the thermal inertial parameter for the matrix heat bath allowed unhindered energy transfer between the heat bath and the matrix molecules, whereas the thermal inertial parameter for the heat bath of guest species prevented the direct heat flow to the guest particle. Therefore, heat transfer to the guest particle was only possible through its interaction with the matrix molecules.

TABLE 1: Comparison of Interatomic Distances from Equilibrated Structures in CHARMM Simulations and from X-ray Diffraction Structures[40,41] The Notations ′ and ″ Represent Atoms in Molecules M′ and M″. Subscripts *x* and *z* Represent Atoms in Molecules M_x and M_z with Unit Translations in the *x* and *z* Directions

atom pair	distance from simulation (Å)	distance from X-ray diffraction (Å)	difference (Å)
O_1-N'	2.823	2.664	0.159
O_2-N'	3.319	3.256	0.063
O_2-C_1'	3.289	3.265	0.024
O_1-C_1'	3.562	3.540	0.022
$O_1''-_zO_2$	3.545	3.742	0.197
$O_1-_xC_4$	3.695	3.795	0.100
$O_1''-O_2$	3.882	3.883	0.001

In the desorption simulations the typical time-step size was 1 fs and the trajectories were recorded at every 0.1 ps for further analysis. The calculations were performed on Indigo2/R4400 and Indy/R4600 workstations (Silicon Graphics, Mountain View, CA) under IRIX 5.3 and IRIX 6.2 operating systems and on a Sun Ultra Enterprise 4000 system (Sun Microsystems, Mountain View, CA) equipped with SunOS 5.5.1 operating system. The SCARECROW trajectory visualization package (Centre for Scientific Computing, Espoo, Finland) was used to animate and evaluate particle histories.[46]

Results and Discussion

1. The Host Crystal. To confirm the validity of the interaction potentials (including the selection of partial charges) and the soundness of other approximations in the model, we calculated some characteristic properties of the crystal structure and the relevant thermal properties of nicotinic acid. Starting from the experimental structure, equilibrium simulations at 300 K showed that the model host system preserved the main features of the crystal. Comparison of the intermolecular distances from the simulation and from X-ray diffraction structure (presented in Table 1) shows that the root-mean-square deviation between our average structure and the X-ray crystal structure is 0.36 Å. The maximum relative error observed between the atomic distances in the simulation and the X-ray structure is 6%. The nicotinic acid molecule, M, in the unit cell is related to the molecule M′ by the screw axis ($^1/_2$,*y*,$^1/_2$) and to the molecule M″ by the symmetry center ($^1/_2$,$^1/_2$,$^1/_2$).[40]

One of the most relevant thermal quantities in the description of laser-induced phase transition is the enthalpy of sublimation, ΔH_{subl}. This quantity was calculated by subtracting the enthalpy of the host crystal in equilibrium configuration from the enthalpy of the system with one nicotinic acid molecule translated from bulk into vacuum. The enthalpy of sublimation for nicotinic acid obtained from the simulation at 300 K was 93 ± 1 kJ/mol, whereas the experimental value was 123.4 kJ/mol.[47] This represents a 25% negative deviation. Underestimating the sublimation energy in the model means that a smaller amount of deposited laser energy is sufficient to induce substantial evaporation at a lower temperature. The constant pressure heat capacity, C_p, of the host crystal can be calculated from the enthalpy fluctuations of the system:

$$\langle \delta H^2 \rangle = k_{\mathrm{B}} T^2 C_p \qquad (2)$$

At room temperature the calculated heat capacity, 134 ± 30 J/(mol·K), compared favorably with the 150 J/(mol·K) typical heat capacity value of similar molecular solids.[22] The notable similarities between structural and thermal properties obtained by the MD model and the experiments ensure that the model represents the most pertinent features of the host crystal.

2. Matrix-Embedded Guest Species. Efficient embedding of guest particles into the host crystal is considered crucial for successful MALDI of macromolecules. The local environment provided by the matrix crystal, however, is radically different from the natural aqueous environment of proteins. Thus, the conformation and the charge state of guest molecules are expected to be different from those observed in water.

The host−guest model systems were obtained by inserting a stretched leucine enkephalin particle (protonated or zwitterionic) into the equilibrated matrix crystal parallel to the hydrogen-bonded nicotinic acid layers. To explore the room-temperature structure of the combined systems, 10 ps molecular dynamics simulations were performed at 300 K. During the equilibrium simulation, displacements of the neighboring host molecules and relaxation of the guest species were observed.

Figure 1 shows the average conformation of a zwitterionic leucine enkephalin molecule buried at 10 Å depth below the surface of the matrix crystal. Initially, the leucine enkephalin molecule was accommodated in plane with a layer of the matrix molecules. During the simulation some of the peptide side chains occasionally extended into neighboring layers. As seen in Figure 1, the nicotinic acid molecules below the guest species retained their initial position, whereas those around and above the guest molecule were displaced, leading to local disorder. The embedded zwitterionic leucine enkephalin exhibited a stretched conformation with intramolecular hydrogen bonds between the carbonyl oxygen and the amide hydrogen atoms of neighboring peptide bonds. Since the nicotinic acid molecules formed hydrogen bonds with molecules in the same layer, we rarely observed hydrogen bonds between the guest molecule and the nicotinic acid molecules from different layers. However, up to 5 hydrogen bonds were observed between the guest molecule and the nicotinic acid molecules within the same layer. The average end-to-end distance of the guest species was 16.9 ± 0.3 Å, significantly larger than both the 7.6 ± 1.5 Å value determined in water and the 2.6 ± 0.1 Å value calculated in a vacuum at the same temperature.

Since the charge state of the guest species in MALDI samples is unclear, we also studied the protonated leucine enkephalin molecule in the nicotinic acid host crystal. A guest molecule, protonated on the amino terminus, was inserted parallel to the hydrogen-bonded layers of the host crystal. As in the case of the zwitterionic molecule, intramolecular hydrogen bonds were observed on the peptide backbone. Similarlly to the zwitterionic molecule, the 16.4 ± 0.3 Å end-to-end distance of the protonated leucine enkephalin was larger than the 7.4 ± 1.9 Å obtained in water and the 4.8 ± 0.2 Å value determined in a vacuum.

3. Host−Guest Systems with Laser Excitation. Ultraviolet (UV) MALDI involves electronic excitation of the matrix followed by internal conversion leading to highly excited vibrational states within the first few picoseconds of illumination. Infrared (IR) MALDI is believed to start with energy deposition directly into certain vibrational degrees of freedom of the matrix. Thus, in both UV and IR MALDI a strongly nonequilibrium situation develops whereby most of the deposited energy is concentrated in the vibrational modes of the matrix. To simulate the effect of laser irradiation, an instantaneous temperature jump was imposed on the equilibrated host−guest system. Different laser irradiances were represented by different increases in temperature. Velocities following the Maxwell−Boltzmann distribution at the final temperature were assigned to all matrix atoms in the system. Experimenting with

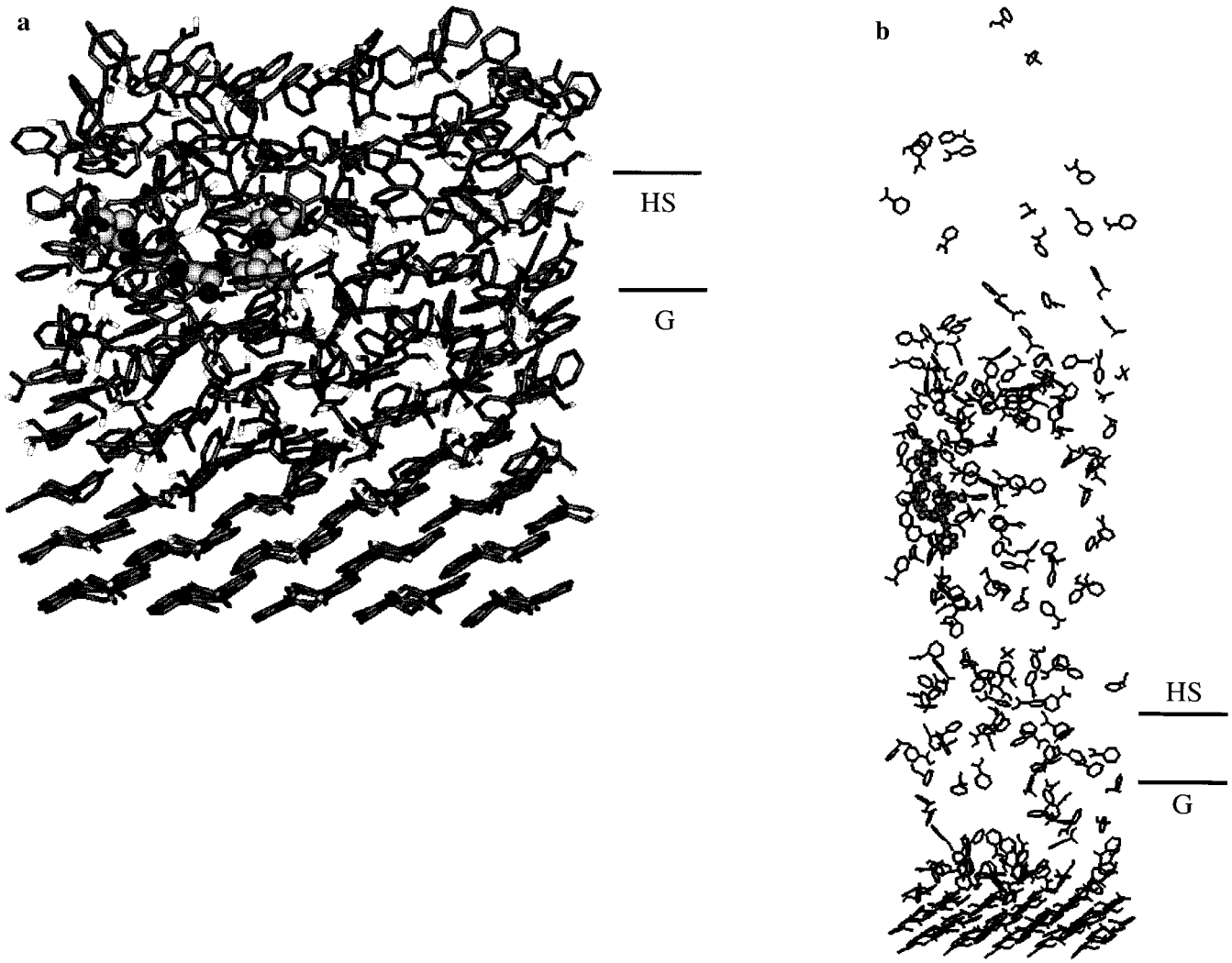

Figure 2. (a) Desorption of leucine enkephalin molecule embedded at 10 Å in nicotinic acid crystal at 1 ps simulation time after adiabatic heating to 1500 K. (b) Ejection of the guest molecule is observed at the 10 ps stage of the simulation. HS and G are defined in the caption of Figure 1.

final temperatures provided a desorption threshold between 1100 and 1500 K. The 1500 K system initially expanded, and after ~1 ps some of the excited molecules moved away from the surface (Figure 2a). The observed sequence of initial expansion followed by acceleration in our simulation is consistent with the basic assumption of the breathing sphere model.[32] While in the breathing sphere approximation the extent and dynamics of expansion are input parameters, our model makes no specific assumptions on these features.

As a result of the 2D periodic boundary condition, only vertical expansion and migration was described. This was a reasonable approximation for the initial stage of desorption in the center of the focal area illuminated by a TEM_{00} beam, where the lateral irradiance gradient was negligible. There was an upper time limit in the simulations determined by the boundary condition interfacing the bottom of the modeled region to the bulk of the crystal. At ~80 ps into the 1500 K simulation the displacement of layers reached the nicotinic acid molecules adjacent to the two fixed layers of the host crystal. At this point the aspect ratio (height/width) exceeded ~15, and the molecules next to the boundary did not drift in the *z* direction. This indicated that beyond this stage the expansion was significantly influenced by the bottom boundary condition.

Figure 2b shows the host−guest system 10 ps after the initial matrix temperature jump to 1500 K. At this stage, some of the hot matrix molecules were ~124 Å ahead of the original surface and ~81 Å ahead of the leucine enkephalin molecule, whereas the less energetic matrix molecules were left behind. This fractionation phenomenon had important consequences for the host−guest energy-transfer process (see discussion in section 6). In the following sections a quantitative description is provided for some aspects of the MALDI process at the molecular level.

4. Liftoff Velocities. In a host−guest system produced by cocrystallization, the guest particles are embedded at different depths. To uncover the effect of guest location with respect to the position of the illuminated surface, we studied the influence of burial depth on liftoff velocities. Three different systems were selected containing zwitterionic guest molecule with the host crystal heated to 1100 and 1500 K and protonated leucine enkephalin molecule in a host environment heated to 1500 K. The two different temperature jumps represented different laser irradiances, whereas the two guest species corresponded to different ionization mechanisms. During the 100 ps simulation the velocities of both host and guest molecules fluctuated around constant values. The average liftoff velocity values are presented in Table 2 for different guest burial depths and for different layers of nicotinic acid. As the burial depth increased from 5 to 20 Å, a significant decrease was observed in the liftoff velocities of both the guest and the host species.

The laser-induced temperature jump had an important effect on guest liftoff velocities. The liftoff velocities of the zwitte-

TABLE 2: Liftoff Velocities of Guest and Matrix Molecules in Leucine Enkephalin−Nicotinic Acid Systems During a 80 ps Simulation

	liftoff velocity (m/s)				
	$T = 1100$ K		$T = 1500$ K		
burial depth (Å)	host	zwitterionic guest	host	zwitterionic guest	protonated guest
1.6	539		1098		
5.0	409	349	852	852	765
8.2	321		690		
10		333		692	537
11.5	255		487		
14.8	150		385		
15		205		371	330
18.2	81		268		
20		10		207	−13
21.6	60		133		
24.9	19		38		

rionic leucine enkephalin molecule at 1100 K (shown in Table 2) are consistently lower than the corresponding values at 1500 K. An increase in the temperature from 1100 K to 1500 K resulted in doubling of the liftoff velocities for the same burial depth and charge state of the guest molecule.

There is corroborating experimental evidence that links the width of velocity distributions to the depth of embedding and/or surface temperatures. It is frequently observed that peak shapes in TOF-MS are sharpest at threshold laser irradiance and deteriorate above it. The threshold laser intensity provides the thinnest possible sampling volume for the desorbed guest molecules and at the same time leads to the lowest surface temperature. Increasing the laser irradiance results in the release of guest particles from larger depths and in higher surface temperatures. According to our model, both of these effects lead to wider velocity distributions and to corresponding peak broadening.

Experimental neutral guest velocity distributions, reported by different groups, show a spread between 0 and ∼1000 m/s. Thus, the observed velocity distributions spread over a range similar to our simulations at 1500 K (−13 m/s < v_{guest} < 765 m/s). It is important to note that the velocity spread associated with the burial depth distribution is dependent on the temperature jump (compare 1100 and 1500 K data in Table 2). Therefore, measuring the guest velocity distributions at different laser irradiances and/or different substrate temperatures can help in testing the validity of the model. If the guest velocity distributions are linked to the different burial depths, lower laser irradiances should lead to smaller spread in velocities. In addition, due to the uneven lateral distribution of laser intensity in the focal spot, different areas of the sample reach different maximum temperatures. Our simulations show that this effect also contributes to significant variations in liftoff velocities. Therefore, the depth of embedding of guest molecules and the laser irradiance variations in the focal area both may contribute to the observed liftoff velocity spread in MALDI.

Measured neutral and ion velocity distributions are available in the literature for both matrix and guest particles in MALDI.[33,48,49] Studies on velocity distributions of neutral gramacidin S and ferulic matrix molecules showed similar distributions for both molecules with 300 m/s < V_{max} < 400 m/s.[48] These velocities were close to the values predicted by the hydrodynamic model.[23] Experimental velocity distributions of different guest molecular ions have shown a mass-independent maximum at ∼750 m/s. However, the velocity of the sinapinic acid matrix ions was reported to be substantially higher than that of the guest molecules (i.e., ∼1140 m/s).[49]

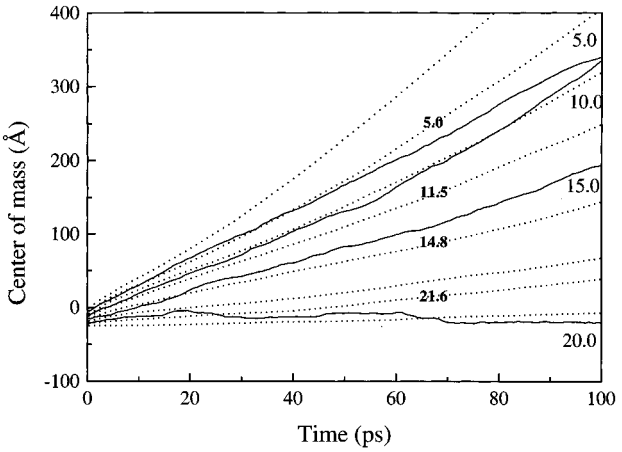

Figure 3. Center-of-mass positions for host and zwitterionic guest molecules at various embedding depths in a 1100 K bath. The positions for each layer of nicotinic acid molecules are shown by dashed lines, whereas the guest molecule displacements are denoted by solid lines.

Caution is required, however, when comparing velocities measured and calculated by different methods. Postionization measurements are typically made on the ∼5 μs time scale, and hydrodynamic calculations are conducted on the ∼100 ns scale, whereas the time span of MD simulations usually does not extend beyond ∼100 ps. The direct comparison of velocities obtained by MD and by experiments hinges on plume densities. If the laser irradiance is low enough to stay in the low plume density regime, i.e., collisions cease in less than ∼1 ns, the MD velocities may be compared to experimental values. If, however, higher plume densities are generated, the MD results can only serve as initial conditions for the hydrodynamic treatment.[23]

The charge state of the guest species in the host is one of the unresolved problems in MALDI. By modeling the desorption of both the zwitterionic and the protonated molecules, we expected to correlate the guest velocity distributions with the nature of the desorbed species. Comparison of the zwitterionic and protonated guest molecules at 1500 K final matrix temperature revealed that the zwitterionic leucine enkephalin molecule has a slightly higher velocity (generally by 10−30%) than the protonated molecule under similar heating conditions and burial depths. A significant difference was observed in liftoff velocities at 20 Å burial depth, where the protonated molecule did not escape from the matrix surface. The lower velocity of protonated guest molecules may be due to the more pronounced host−guest interactions or to the differences in conformation dynamics between the considered guest species (see section 5). The velocity values for both the zwitterionic and protonated guest molecules, however, are close to the values observed for host molecules at similar burial depths. For neutral molecules, it has been reported that the means of both the guest and the host velocity distributions are close to the expansion velocity of the plume.[49]

Figure 3 shows the center-of-mass displacement of a zwitterionic leucine enkephalin molecule (solid line) and layers of nicotinic acid molecules (dashed line) along the z axis during the 100 ps simulation for 1100 K final matrix temperature. The center-of-mass displacements along the z axis indicate the rapid evaporation of surface molecules. Particles originating from deeper layers attain consistently lower velocities. Moreover, Figure 3 shows that the guest molecules buried at 20 Å do not escape from the matrix during the 100 ps simulation. To compare the departure of host and guest molecules, the matrix molecules are grouped according to layers. The burial depth

dependence of matrix departure velocities shows a monotonic behavior. It can be seen that even though the entire system is heated evenly, matrix molecules evaporate in a layer-by-layer manner. During the time scale of our calculations, the different layers do not mix. This mechanism corresponds to surface evaporation, an unexpected phenomenon given the large degree of overheating due to rapid energy deposition. Comparing the displacement of leucine enkephalin and nicotinic acid particles in Figure 3, it is observed that the guest molecule has a liftoff velocity close to that of the matrix molecules at similar burial depth. Due to the uniform desorption velocity of most molecules within a layer, molecular collisions do not result in a net momentum change in the vertical direction.

5. Guest Species Conformation Changes. Extensive conformational studies of leucine enkephalin have shown that in the solid state this molecule exists in three different conformations: extended, single-bend (type I′ β-bend), and pleated β-sheet.[50−52] Gas-phase conformational data, however, are not available for direct comparison with MD calculations. We have investigated the conformation of the guest molecule, leucine enkephalin, during and after the desorption from the matrix host crystal. End-to-end distances and intramolecular hydrogen bonds are followed to describe the conformation changes induced by the phase transition. Although end-to-end distances do not capture all aspects of the protein conformation, the peptide molecule investigated in this study is sufficiently short to utilize this measure as an important descriptor of the secondary structure.

The initial conditions for the guest conformation calculation are defined by the equilibrated conformation in the crystalline host. The end-to-end distance of the extended zwitterionic molecule in the host crystal was ∼16.9 ± 0.3 Å. This value is close to the observed distances between the nitrogen in the amino terminus group and the two oxygens in the carboxylic group by X-ray crystallography in the extended conformation, 15.3 and 16.8 Å. In ∼15 ps, the end-to-end distance of the zwitterionic guest molecule decreases to 2.6 ± 0.1 Å (Figure 4a). After the conformation change, small fluctuations were observed in the end-to-end distance, indicating that the end-to-end coupling driven by the Coulomb interaction is relatively strong in this molecule. After escaping the surface of the matrix and reaching the folded structure, the leucine enkephalin molecule maintains a more stable conformation during the rest of the desorption process. Changes in the burial depth did not seem to effect the gas-phase end-to-end distances of the guest molecules.

To compare the folded structure with the β-bend structure, we monitored the two important intramolecular hydrogen bonds. The hydrogen bonds formed between the nitrogen of Phe and the carboxyl oxygen of Tyr (bond A) and between the nitrogen of the Tyr and the carbonyl oxygen of Phe (bond B). During the desorption process, bond B is formed and is relatively stable for more than 40 ps of the simulation. However, the distance between the oxygen in Tyr and the nitrogen in Phe is higher than the expected value in this conformation (∼6 Å vs 3.0 Å). It is important to consider the major differences in the molecular environments in this comparison. During the desorption process the leucine enkephalin spends most of its time in the gas-phase surrounded by matrix molecules, whereas the X-ray data are obtained from crystalline leucine enkephalin.

In comparison, the protonated molecule reached a higher gas-phase end-to-end distance, 4.8 ± 0.2 Å, in a longer time, ∼25 ps (Figure 4b). Compared to the zwitterionic case, larger conformational fluctuations were observed. These differences

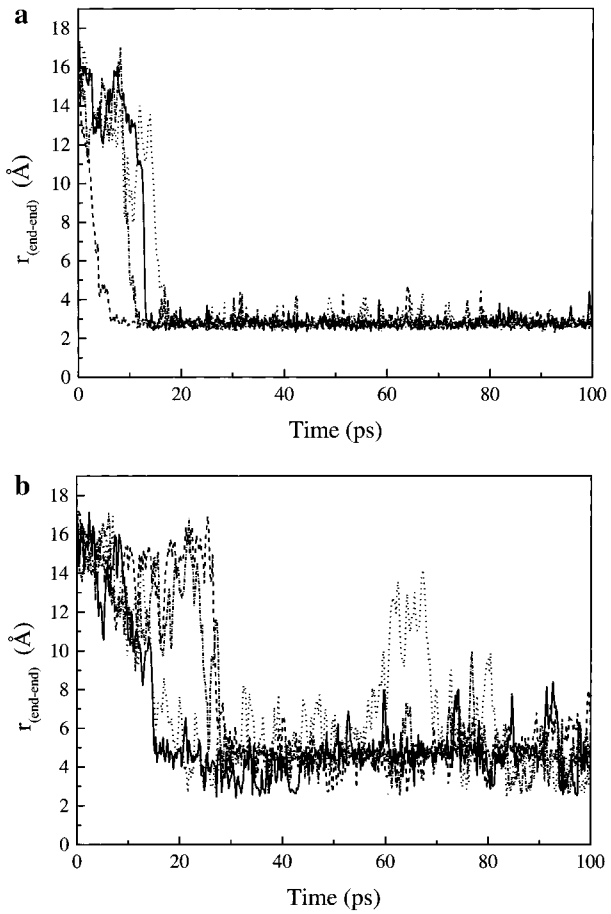

Figure 4. End-to-end distances of (a) zwitterionic and (b) protonated leucine enkephalin molecule during the desorption at 1500 K. The solid, dashed, dotted, and dashed−dotted lines represent systems with initial burial depths of 5, 10, 15, and 20 Å, respectively.

are the consequence of much weaker Coulomb interaction between the end groups in the protonated molecule. The lack of dominant end-to-end attraction leads to stronger interactions between the protonated guest molecule and the host molecules. Conversely, stronger interactions between the two end groups in the zwitterionic molecule make interactions with the host molecules less likely.

Comparison of the intramolecular hydrogen bonds shows that once the protonated guest molecule is desorbed (after ∼27 ps) bond B becomes stable with a bond length of ∼3.0 ± 0.8 Å. The distance between the nitrogen in Tyr and the oxygen in Phe for the protonated molecule becomes shorter then the observed value for the zwitterionic molecule (4.7 ± 0.9 Å vs 5.9 ± 1.1 Å). Despite the weaker interaction between the end groups in the protonated molecule, the side chains have a more stable interaction than in the zwitterionic molecule.

6. Host−Guest Energy Transfer during Desorption. The observation of mild but varying degree of fragmentation in MALDI due to different laser parameters, guest molecules, matrixes, and observation time scales has prompted the investigation of energy transfer between the matrix and guest molecules.[53−55] To follow the translational and vibrational heating of guest molecules, we calculated the particle temperature histories as a function of burial depth in three different systems: zwitterionic guest molecules in 1100 and 1500 K environments and protonated species in a 1500 K bath. Table 3 shows the kinetic temperatures of both matrix and guest molecules and the internal temperatures of the guest molecules as a function of burial depth. The kinetic temperatures of the

TABLE 3: Calculated Average Matrix and Guest Molecule Temperatures Attained in the 80 ps Simulation

	temperature (K)							
	bath = 1100 K			bath = 1500 K				
burial depth (Å)	host (kinetic)	zwitterionic guest (kinetic)	zwitterionic guest (internal)	host (kinetic)	zwitterionic guest (kinetic)	protonated guest (kinetic)	zwitterionic guest (internal)	protonated guest (internal)
5.0	1099 ± 21	1091 ± 168	842 ± 155	1500 ± 28	1610 ± 180	1491 ± 167	940 ± 155	910 ± 137
10.0	1101 ± 22	1072 ± 149	835 ± 147	1497 ± 29	1477 ± 181	1318 ± 174	947 ± 158	915 ± 145
15.0	1097 ± 22	980 ± 147	788 ± 134	1499 ± 28	1232 ± 158	1231 ± 184	944 ± 155	966 ± 173
20.0	1100 ± 21	1073 ± 164	892 ± 155	1501 ± 28	1217 ± 162	1112 ± 152	953 ± 161	917 ± 146

matrix molecules are essentially constant and independent of the burial depth. The calculated values are very close to the temperature of the heat bath in contact with the matrix molecules.

As the guest burial depth increases, however, a decrease in its kinetic temperature is seen in almost all cases. Since the modeled volume consists of only one guest molecule and many matrix particles, the observed temperature fluctuations are much higher for the guest than for the matrix molecules. As we have mentioned in section 4, the guest molecules embedded close to the surface are accompanied by energetic matrix molecules, i.e., by the ones that have higher liftoff velocities. The higher kinetic temperature of shallow-embedded guest molecules is due to this "hotter" environment throughout the desorption process.

The zwitterionic molecule positioned at 20 Å below the surface in the 1100 K case substantially deviates from the trend established in the previous paragraph. This discrepancy is due to the fundamentally different trajectory of this particle. Inspecting Figure 3, it is apparent that this guest molecule does not escape from the matrix; therefore, it remains confined in the higher density environment where frequent collisions with the matrix molecules facilitate the energy transfer.

We have also investigated the variations in the internal temperatures of guest molecules (see Table 3). The internal temperatures of the guest molecules in all three cases are significantly lower than the matrix or heat bath temperatures. At 1500 K the internal temperature values are very similar for the two different charge states. Lowering the heat bath temperature to 1100 K results in somewhat lower guest internal temperatures. The 400 K bath temperature difference, however, only leads to ~100 K guest internal temperature change. This observation is a clear indication of hindered energy transfer between matrix and guest molecules. It is interesting to note that despite strong correlation with velocity, the burial depth has almost no influence on guest internal temperature. The consistently lower postdesorption internal energies of the guest species may account for the lack of thermodecomposition in MALDI.

Some models in the literature suggest that in MALDI a pressure pulse is generated and this pulse can be viewed as the basis of particle ejection.[24] In light of our results, it is hard to separate this pressure pulse from the temperature spike caused by the laser irradiation. Although the velocity does change from zero average to a finite value at the irradiance threshold, this can be viewed both as the consequence of the pressure pulse and as the result of exceeding the phase transition temperature. We plan to expand our investigations to include different matrixes and other peptide and oligonucleotide guest molecules to see if the related experimental findings (matrix dependence of guest internal temperatures, lower stability of oligonucleotides, etc.) are corroborated by the model.

Acknowledgment. This work was supported by the National Science Foundation (Grant No. NSF-CHE-9523413). The authors express their appreciation to Dr. A. Bencsura for helpful discussions on the fine points of implementing the CHARMM code for crystal environments.

References and Notes

(1) Lubman, D. M. *Lasers and Mass Spectrometry*; Oxford University: New York, 1990.
(2) Karas, M.; Bachmann, D.; Bahr, U.; Hillenkamp, F. *Int. J. Mass Spectrom. Ion Processes* **1987**, *78*, 53.
(3) Karas, M.; Hillenkamp, F. *Anal. Chem.* **1988**, *60*, 2299.
(4) Zenobi, R.; Zare, R. N. In *Advances in Multiphoton Spectroscopy and Processes*; Lin, H. S., Ed.; World Scientific: Singapore, 1991; Vol. *7*, pp 1-44.
(5) Vertes, A.; Gijbels, R.; Adams, F. *Laser Ionization Mass Analysis*; Wiley: New York, 1993.
(6) Rizzo, T. R.; Levy, D. H. In *Lasers and Mass Spectrometry*; Lubman, D. M., Ed.; Oxford University: New York, 1990; pp 402−422.
(7) Li, L.; Hogg, A. H.; Wang, A. P. L.; Zhang, J.; Nagra, D. S. *Anal. Chem.* **1991**, *63*, 974.
(8) von Helden, G.; Wyttenbach, T.; Bowers, M. T. *Science* **1995**, *267*, 1483.
(9) Wyttenbach, T.; von Helden, G.; Bowers, M. T. *J. Am. Chem. Soc.* **1996**, 118, 8355.
(10) von Helden, G.; Wyttenbach, T.; Bowers, M. T. *Int. J. Mass Spectrom. Ion Processes* **1995**, *146/147*, 349.
(11) Chan, T. W. Dominic; Colburn, A. W.; Derrick, P. *J. Org. Mass Spectrom.* **1992**, *27*, 53.
(12) Tang, K.; Taranenko, N. I.; Allman, S. L.; Chen, C. H.; Chang, L. Y.; Jacobson, K. B. *Rapid Commun. Mass Spectrom.* **1994**, *8*, 673.
(13) Wu, J. K.; Steding, A.; Becker, C. H.; *Rapid Commun. Mass Spectrom.* **1992**, *7*, 142.
(14) Brown, R. S.; Lennon, J. J. *Anal. Chem.* **1995**, *67*, 1998.
(15) Vestal, M. L.; Juhasz, P.; Martin, S. A. *Rapid Commun. Mass Spectrom.* **1995**, *9*, 1044.
(16) Beavis, R. C.; Chait, B. T. *Anal. Chem.* **1990**, *62*, 1836.
(17) Juhasz, P.; Biemann, K. *Proc. Natl. Acad. Sci. U.S.A.* **1994**, *91*, 4333.
(18) Tang, X.; Callahan, J. H.; Zhou, P.; Vertes, A. *Anal. Chem.* **1995**, *67*, 4542.
(19) Preston-Schaffter, L. M.; Kinsel, G. R.; Russell, D. H. *J. Am. Soc. Mass Spectrom.* **1994**, *5*, 800.
(20) Dreisewerd, K.; Schurenberg, M.; Karas, M.; Hillenkamp, F. *Int. J. Mass Spectrom. Ion Processes* **1995**, *141*, 127.
(21) Gorman, G. S.; Speir, J. P.; Turner, C. A.; Amster, I. J. *J. Am. Chem. Soc.* **1992**, *114*, 3986.
(22) Vertes, A.; Gijbels, R.; Levine, R. D. *Rapid Commun. Mass Spectrom.* **1990**, *4*, 228.
(23) Vertes, A.; Irinyi, G.; Gijbels, R. *Anal. Chem.* **1993**, *65*, 2389.
(24) Johnson, R. E., *Int. J. Mass Spectrom. Ion Processes* **1994**, *139*, 25.
(25) Knochenmuss, R.; Dubois, F.; Dale, M. J.; Zenobi, R. *Rapid Commun. Mass Spectrom.* **1996**, *10*, 871.
(26) Vertes, A.; Levine, R. D. *Chem. Phys. Lett.* **1990**, *171*, 284.
(27) Holme, T. A.; Levine, R. D. *Surf. Sci.* **1989**, *216*, 587.
(28) Taylor, R. S.; Garrison, B. J. *Chem. Phys. Lett.* **1994**, *230*, 495.
(29) Zajac, R.; Chakrabarti, A. *J. Chem. Phys.* **1996**, *104*, 2418.
(30) Bencsura, A.; Vertes, A. *Chem. Phys. Lett.* **1995**, *247*, 142.
(31) Bencsura, A.; Navale, V.; Sadeghi, M.; Vertes, A. *Rapid Commun. Mass Spectrom.* **1997**, *11*, 679.
(32) Zhigilei, L. V.; Kodali, P. B. S.; Garrison, B. J. *J. Phys. Chem. B* **1997**, *101*, 2028.
(33) Ens, W.; Mao, Y.; Mayer, F.; Standing, K. G. *Rapid Commun. Mass Spectrom.* **1991**, 5, 117.
(34) Allwood, D. A.; Perera, I. K.; Perkins, J.; Dyer, P. E.; Oldershaw, G. A. *Appl. Surf. Sci.* **1996,** *103*, 231.
(35) Valentine, S. J.; Counterman, A. E.; Clemmer, D. E. *J. Am. Soc. Mass Spectrom.* **1997**, *8*, 954.

(36) Katta, V.; Chait, B. T. *Rapid Commun. Mass Spectrom.* **1991**, *5*, 214.
(37) Covey, T.; Douglas, D. J. *J. Am. Soc. Mass Spectrom.* **1993**, *4*, 616.
(38) Brooks, B. R.; Bruccoleri, R. E.; Olafson, B. D.; Swaminathan, S.; Karplus, M. *J. Comput. Chem.* **1983**, *4*, 187.
(39) Schmidt, M. W.; Baldridge, K. K.; Boatz, J. A.; Elbert, S. T.; Gordon, M. S.; Jensen, J. J.; Koseki, D.; Matsunaga, N.; Nguyen, K. A.; Su, S.; Windus, T. L.; Dupuis, M.; Montgomery, J. A. *J. Comput. Chem.* **1993**, *14*, 1347.
(40) Wright, W. B.; King, G. S. D. *Acta Crystallogr.* **1953**, *6*, 305.
(41) Gupta, M. P.; Kumar, P. *Cryst. Struct. Commun.* **1975**, *4*, 365.
(42) Allen, M. P.; Allen, D. J. *Computer Simulation of Liquids*; Clarendon Press: Oxford, 1989
(43) Beavis, R. C.; Bridson, J. N. *J. Phys. D* **1993**, *26*, 442.
(44) Nose, S. *J. Chem. Phys.* **1984**, *81*, 511.
(45) Hoover, W. G. *Phys. Rev.* **1985**, *31*, 1695.
(46) Laaksone, L. *J. Mol. Graph.* **1992**, *10*, 33.
(47) Bickerton, J.; Pilcher, G.; Al-Takhin, G, *J. Chem. Thermodyn.* **1984**, *16*, 373.
(48) Huth-Fehre, T.; Becker, C. H. *Rapid Commun. Mass Spectrom.* **1991**, *5*, 378.
(49) Beavis, R. C.; Chait, B. T. *Chem. Phys. Lett.* **1991**, *181*, 479.
(50) Karle, I. L.; Karle, J.; Mastropaolo, D.; Camerman, A.; Camerman, N. *Acta Crystallogr.* **1983**, *B39*, 625.
(51) Smith, G. D.; Griffin, J. F. *Science* **1978**, *199*, 1214.
(52) Aubry, A.; Birlirakis, N.; Sakarellos-Daitsiotis, M.; Sakarellos, C.; Marraud, M. *Biopolymers* **1989**, *28*, 27.
(53) Qin, J.; Steenvoorden, R. J.; Chait, B. T. *Proceedings of the 42nd ASMS Conference on Mass Spectrometry and Allied Topics*; Chicago, IL, 1994; p 5.
(54) Kinsel, R. K.; Preston, L. M.; Russell, D. H. *Rapid Commun. Mass Spectrom.* **1994**, *21*, 205.
(55) Amft, M.; Grundwürmer, J. M.; Grotemeyer, J. *Proceedings of the 44th ASMS Conference on Mass Spectrometry and Allied Topics*; Portland, OR, 1996; p 1352.